Engineering Geology 207 (2016) 115–128

Contents lists available at ScienceDirect

Engineering Geology

journal homepage: www.elsevier.com/locate/enggeo

Investigating the reliability of H/V spectral ratio and image entropy for quantifying the degree of disintegration of weak rocks

Orlando Rincon [a], Abdul Shakoor [b,*], Manuel Ocampo [c]

[a] Department of Civil Engineering, Universidad de la Salle, Bogotá, Colombia
[b] Department of Geology, Kent State University, Kent, OH 44242, USA
[c] Department of Civil Engineering, Pontificia Universidad Javeriana, Bogotá, Colombia

ARTICLE INFO

Article history:
Received 9 June 2015
Received in revised form 17 March 2016
Accepted 17 April 2016
Available online 21 April 2016

Keywords:
Weak rocks
Entropy
Image analysis
Microtremor H/V ratio

ABSTRACT

Characterization and quantification of disintegration behavior of weak rocks, such as shales, claystones, mudstones, and siltstones, are usually a difficult task because of their extremely diverse nature. These rocks present numerous stability problems along cut slopes around the world because they can change rapidly from rock-like to soil-like materials upon exposure to natural climatic conditions. Engineers often overestimate the design parameters for cut slopes in these rocks when laboratory tests are performed on fresh samples. Adjusting the design parameters for the anticipated amount of disintegration can be problematic because of the complex and time-dependent nature of disintegration behavior. In this study, we investigate the reliability of using microtremor H/V spectral ratio, derived from microtremor signals, and image entropy, obtained from image analysis techniques, for quantifying the varying degrees of disintegration. During 2011–2014, both techniques were used to study disintegration of slopes cut through claystones, mudstones, and limestones along the 80-km stretch of a highway between Bogotá and Tunja in central Colombia. For image analysis, a new algorithm was developed to discriminate between varying degrees of disintegration across the complete color structure of the image, avoiding the gray-scale transformation that is usually time consuming. The results indicate significant correlations between the degree of disintegration of the cut face, the dominant frequency estimated from the microtremor H/V ratio, and the image entropy values, suggesting that H/V ratio and image entropy can be reliable techniques for quantifying the degree of disintegration.

1. Introduction

Although extensive research has been done on disintegration of week rocks, the disintegration process is not fully understood nor is the transition from rock to soil-like material, upon disintegration, clearly defined. Weak rocks, in varying stages of disintegration, have been designated as intermediate geomaterials (IGMs) by some researchers (Samtani and Nowatzki, 2006; Mokwa and Brooks, 2009; Cruz et al., 2012). Uniaxial compressive strength (UCS) is often used to distinguish between soil and rock. Peck et al. (1974) described hard soil as a material with UCS greater than 400 kPa, whereas the International Society for Rock Mechanics (ISRM) (ISRM, 2007) categorized weak rocks as those with UCS values falling between 250 kPa and 1000 kPa. Mokwa and Brooks (2008) defined the IGMs in terms of both UCS (600–12,500 kPa) and stiffness (100–1000 MPa). They concluded that principles of both soil mechanics and rock mechanics apply to IGM behavior and to engineering design involving these materials. However, UCS is not a reliable basis for classifying weak rocks, especially shales, claystones, and mudstones, because it is greatly influenced by the degree of disintegration. Another disadvantage of using UCS to classify weak rocks or IGMs is that UCS can be relatively high for fresh samples but the rock may still experience rapid disintegration when exposed to natural climatic conditions in a road cut. An alternative to using UCS, that avoids sampling difficulties in cases where the slopes are in advanced states of disintegration, is to use the existing classification schemes such as the slake durability rating (SDR) chart developed by Erguler and Ulusay (2009), the geological strength index (GSI) proposed by Marinos and Hoek (2000), or the empirical methods presented in Dinc et al. (2011). The SDR chart, used in this study, is based on mean fracture frequency (λ) of disintegrated rock, as observed in the field. Fracture frequency (λ) is the inverse of fracture spacing (ISRM, 2007) and SDR $= 100–100 * \lambda$ (Erguler and Ulusay, 2009). The chart was developed on laboratory and field-based observations of disintegration characteristics of different clay bearing rocks. It includes six rating classes, designated as I through VI, with their corresponding disintegration patterns, fracture frequency (λ) values, SDR values, and related information about other physical properties. Table 1 shows the SDR data for each of the six classes, based on the SDR chart. Based on the variation

* Corresponding author.
E-mail address: ashakoor@kent.edu (A. Shakoor).

http://dx.doi.org/10.1016/j.enggeo.2016.04.020

Table 1
Slake durability rating (SDR) data based on SDR chart by Erguler and Ulusay (2009).

Class	Fracture frequency range (λ) (mm^{-1})	Mean fracture frequency (λ) (mm^{-1})	Slake durability rating (SDR) range SDR = 100–100 ∗ λ (%)	Mean slake durability rating (SDR) (%)
IA	0.00–0.00	0.00	100	100.0
IB	0.01–0.05	0.30	95–99	97.5
II	0.05–0.20	0.13	80–94	87.5
III	0.20–0.40	0.30	60–79	70.0
IV	0.40–0.60	0.50	40–59	50.0
V	0.60–0.80	0.70	20–39	30.0
VI	0.80–1.00	0.90	0–19	10.0

of disintegration pattern within class I, it is divided into subclasses IA and IB. Two separate disintegration patterns are included for each of subclass IB and class VI. Using the chart eliminates the need to perform the standardized slake durability index test in the laboratory [American Society for Testing and Materials (ASTM) D4644; ASTM International, 2013], thereby avoiding some of its limitations, as outlined by previous researchers (Goodman, 1989; Santi, 1998; Czerewko and Cripps, 2001; Sadisun et al., 2005; Santi, 2006; Erguler and Shakoor, 2009; Tonnizam et al., 2011; Gautam and Shakoor, 2013). The limitation of the chart is that its use involves personal judgment and, therefore, the results can be subjective.

Microtremors and image entropy can be used in combination with SDR to characterize the changes upon disintegration of weak rocks.

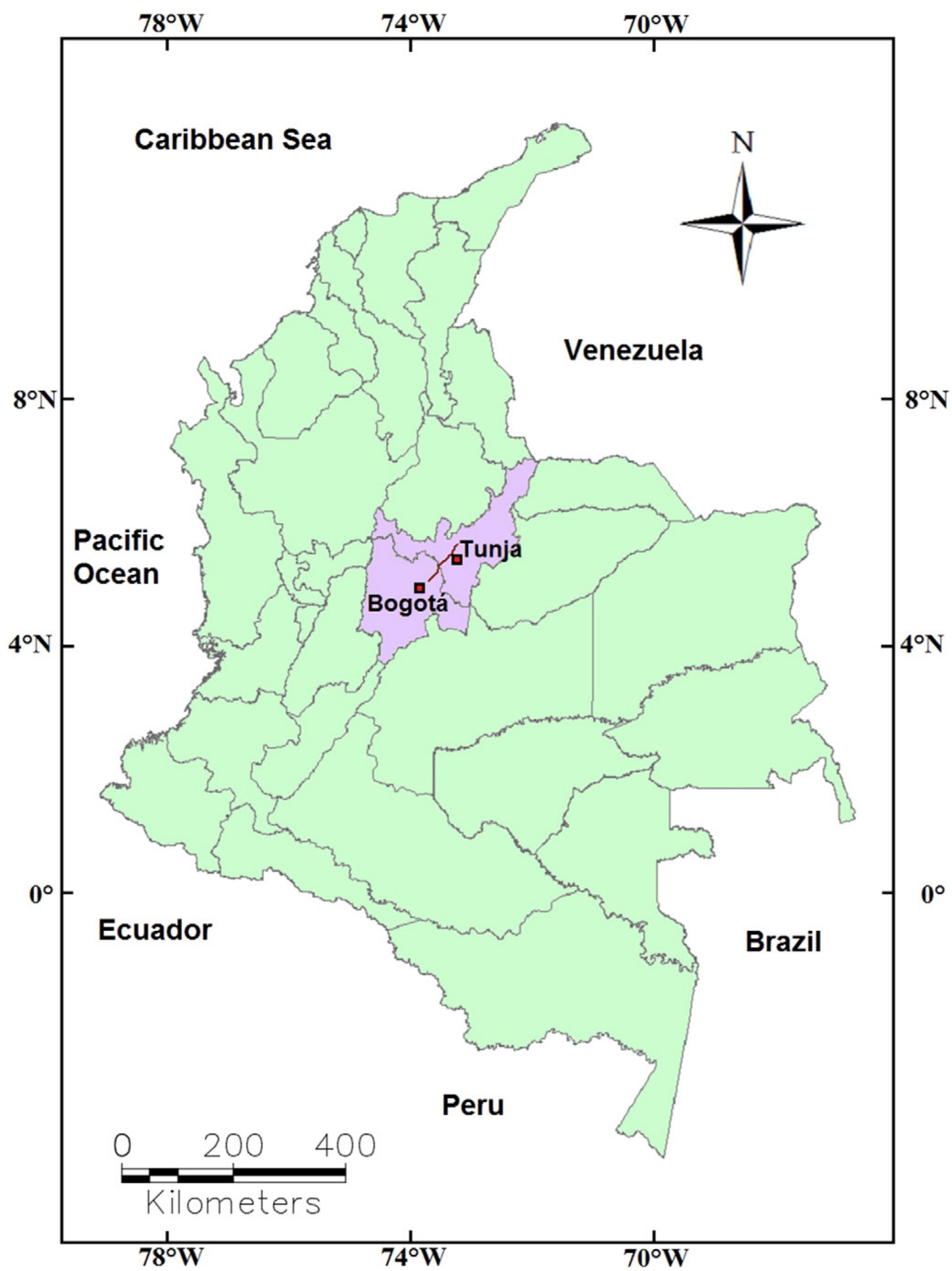

Fig. 1. Location of the study area.

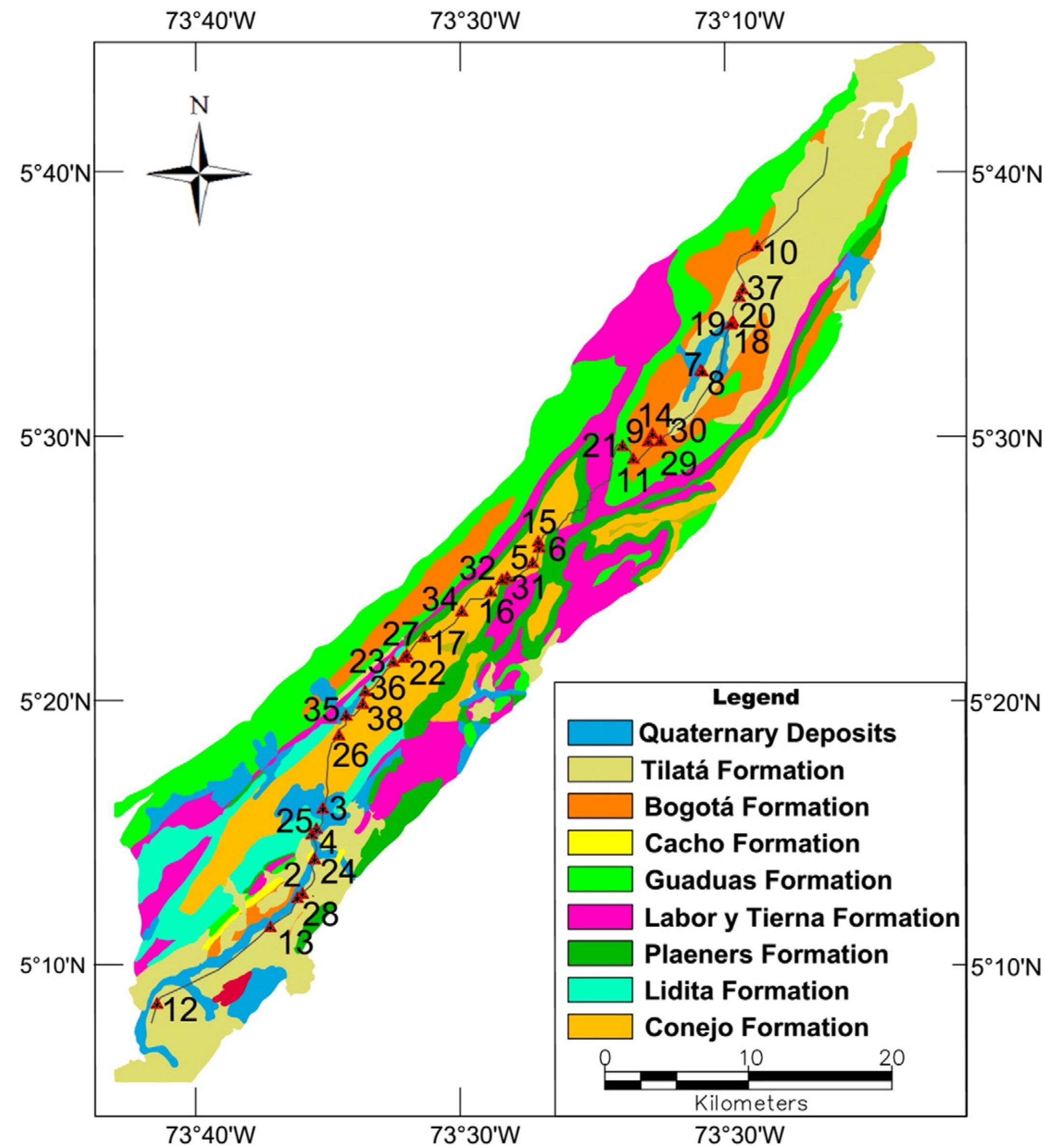

Fig. 2. Geologic map of the study area with the sampling locations along the Bogotá–Tunja highway shown by red triangles.

Microtremors are defined as vibrations with amplitudes between 0.1 and 1.0 μm and periods between 0.05 and 2.0 s (Kanai and Tanaka, 1961). They have been used previously to study the dynamic properties of surface layers of a terrain. Nakamura (1989, 2000) proposed using the ratio of the horizontal (H) to vertical (V) components of the Fourier amplitude spectra, designated as H/V spectral ratio, of the ambient noise vibrations (microtremors) recorded on the surface, for estimating the transference function of the surface layers. He termed the amplitude spectra as the Quasi-Transfer Spectra (QTS), where:

$$QTS = \frac{H_{surface}}{V_{surface}}. \quad (1)$$

The H/V ratio of noise can be used to identify the fundamental resonant frequency and amplification factor of the sediment layers (Nakamura, 1989, 2000). Because of its efficient and cost effective nature, the H/V ratio is a widely used technique in multiple areas of research such as dynamic characterization of soil and rock, earthquake engineering, evaluation of degree of compaction, and other geophysical investigations. (Delgado et al., 2000; Guéguen et al., 2000; Ojeda and Escallon, 2000; Zaslavsky et al., 2000; Ojeda et al., 2002; Parolai et al., 2004; Walling et al., 2009; Dinesh et al., 2010; Mundepi et al., 2010; Rosenblad and Goetz, 2010; Sukumaran et al., 2011; Harutoonian et al., 2012; Ritta et al., 2013; Vella et al., 2013; Clavero et al., 2014; Guo et al., 2014).

Previous studies regarding the use of H/V spectral ratio focused mostly on soil deposits. However, using adequate arrays of measurements, it can provide strong correlations between the nature of weak

Table 2
Geologic formations exposed in the study area.

Formation name	Geologic period	Lithology
Tilatá	Neogene	Claystone, sandstone
Bogotá	Tertiary	Claystone, sandstone, mudstone, siltstone
Guaduas	Cretaceous	Claystone, quartzarenite, coal
Chipaque	Cretaceous	Shale, mudstone
Guadalupe	Cretaceous	Sandstone
Planers	Cretaceous	Siltstone, claystone

Table 3
Location, geologic formation, and rock type data for the samples collected from the 38 sites. Bold indicates the eight sites that were monitored for an extended period.

Site	Latitude	Longitude	Zone	Formation	Rock type
1	N 5.0828	W 73.7263	Sisga	Guaduas	Mudstone
2	**N 5.2107**	**W 73.5991**	**Villa Pinzon**	**Tilatá**	**Siltstone**
3	**N 5.2644**	**W 73.5863**	**Villa Pinzon**	**Bogotá**	**Mudstone**
4	N 5.2481	W 73.5932	Villa Pinzon	Regadera/Bogotá	Mudstone
5	**N 5.4195**	**W 73.4544**	**Ventaquemada**	**Bogotá**	**Mudstone**
6	**N 5.4291**	**W 73.4503**	**Puente de Boyacá**	**Bogotá**	**Mudstone**
7	N 5.5408	W 73.3488	Tunja	Tilatá	Claystone, siltstone
8	**N 5.5408**	**W 73.3488**	**Tunja**	**Tilatá**	**Claystone, siltstone**
9	N 5.4961	W 73.3818	Tunja	Bogotá	Mudstone
10	N 5.6189	W 73.3132	Combita	Bogotá	Mudstone
11	**N 5.4850**	**W 73.3911**	**Runta**	**Bogotá**	**Mudstone**
12	N 5.1414	W 73.6905	Choconta	Tilatá	Mudstone
13	**N 5.1898**	**W 73.6193**	**Villa Pinzon**	**Tilatá**	**Mudstone**
14	N 5.5009	W 73.3790	Tunja	Bogotá	Mudstone
15	N 5.4328	W 73.4509	Puente de Boyacá	Bogotá	Mudstone
16	N 5.4011	W 73.4806	Ventaquemada	Guaduas	Mudstone
17	N 5.3727	W 73.5224	Ventaquemada	Labor y Tierna	Shale, claystone
18	**N 5.5707**	**W 73.3294**	**Tunja**	**Tilatá**	**Claystone, siltstone**
19	N 5.5707	W 73.3294	Tunja	Tilatá	Claystone, siltstone
20	N 5.5718	W 73.3285	Tunja	Tilatá	Claystone, siltstone
21	N 5.4933	W 73.3978	Tunja	Guaduas	Mudstone, shale
22	N 5.3596	W 73.5353	Ventaquemada	Labor y Tierna	Shale, claystone
23	N 5.3571	W 73.5421	Ventaquemada	Plaenners	Siltstone, claystone
24	N 5.2324	W 73.5915	Villa Pinzon	Tilatá	Claystone, siltstone
25	N 5.2515	W 73.5903	Villa Pinzon	Plaenners	Siltstone, claystone
26	N 5.3107	W 73.5762	Albarracin	Conejo	Mudstone
27	N 5.3614	W 73.5336	Ventaquemada	Labor y Tierna	Shale, claystone
28	N 5.2082	W 73.6023	Villa Pinzon	Tilatá	Claystone, siltstone
29	N 5.3305	W 73.3738	Tunja	Bogotá	Claystone, mudstone
30	N 5.4967	W 73.3739	Tunja	Bogotá	Claystone, mudstone
31	N 5.4102	W 73.4704	Ventaquemada	Chipaque	Shale
32	N 5.4088	W 73.4736	Ventaquemada	Chipaque	Shale
33	N 5.5918	W 73.3224	Oicata	Tilatá	Claystone, sandstone
34	N 5.3889	W 73.4990	Ventaquemada	Chipaque	Shale, mudstone
35	N 5.3230	W 73.5717	Ventaquemada	Chipaque	Shale, mudstone
36	N 5.3384	W 73.5597	Ventaquemada	Chipaque	Shale, siltstone, claystone
37	N 5.5870	W 73.3244	Tunja	Tilatá	Claystone
38	N 5.3305	W 73.5612	Ventaquemada	Guaduas	Mudstone

rocks and their disintegration response under natural exposure. In a study involving 32 sites in Canada, Siddiqqi and Atkinson (2002) found that H/V ratio-based interpretations were consistent with general geologic conditions at the sites. They observed that amplification of the H/V ratio increased and the dominant frequency decreased where the geological conditions indicated the presence of weak, soft rocks.

Image analysis is the conversion of an image into a number or a set of numbers that reflects characteristics or changes in characteristics of a material (Heilbronner and Barrett (2013). It can be used to detect changes in texture of weak rocks upon disintegration as new cracks, voids, and irregularities develop and as color alterations occur. Image analysis removes some of the subjectivity of the existing visual classification methods based on predefined patterns. Image entropy, a statistical second order parameter reflecting the homogeneity of the image, is the commonly used parameter for image analysis. The parameter, originally proposed by Shannon (1948) and denoted by the letter H, is defined as:

$$H = \sum_{i=1}^{L} P_i \log_2 P_i \qquad (2)$$

Table 4
Criteria used for classifying disintegration level into low, medium, and high categories.

Degree of disintegration	Slake durability rating	
	Class	SDR (%)
Low	IA, IB, II	100–80
Medium	III, IV	79–40
High	V, VI	39–0

where P_i is the probability of the occurrence of the pixel value i, calculated from the ratio between each histogram cell that contains the observed frequency of the corresponding image intensity value and the total number of pixels in the image. The value of entropy is given in bits.

According to Burger and Burge (2013), entropy is a statistical measure that quantifies the average amount of information contained in the "messages" generated by a stochastic data source. Thus, a number of pixels, N, can be interpreted as a message of N symbols.

From the point of view of disintegration of weak rocks, the message could be associated with the changes in the values of intensities of each color, i.e. red, green, or blue (RGB), of each pixel in the captured image. The changes in entropy reflect modifications in the surface texture due to cracks, fragmentation, and voids. In other words, the interaction of the rock surface with the incident light varies with increasing disintegration and, therefore, the distribution of each color channel in the image is different. These differences are reflected in the intensity histograms of red, blue, and green. The intensity is obtained by adding the average of red, green, and blue values for each pixel.

2. Study objective

The objective of this study was to investigate the usefulness and reliability of microtremor H/V spectral ratio (Nakamura, 1989, 2000) and image entropy for quantifying the degree of disintegration of weak rocks, as compared to the SDR classification by Erguler and Ulusay (2009).

Table 5
Location, formation, SDR, disintegration classification, and fundamental frequency (Hz), based on H/V ratio, for the sites used for microtremor measurements.

Site	Latitude	Longitude	Locality	Slope reach	Formation	SDR class	Disintegration classification	Fundamental frequency (Hz) from H/V ratio
1	N 5.1881	W 73.6212	Villapinzón	Middle	Tilatá	II	Low	21.09
2	N 5.2106	W 73.5985	Villapinzón	Middle	Tilatá	IV	Medium	13.14
3	N 5.2319	W 73.5917	Villapinzón	Lower	Tilatá	III	Medium	5.37
4	N 5.2332	W 73.5913	Villapinzón	Lower	Tilatá	III	Medium	18.88
5	N 5.291	W 73.5837	Albarracin	Lower	Guadalupe	III	Medium	16.46
6	N 5.3227	W 73.571	Albarracin	Middle	Guadalupe	VI	Medium	0.67
7	N 5.3226	W 73.5707	Albarracin	Lower	Guadalupe	III	Medium	18.87
8	N 5.3406	W 73.5553	Ventaquemada	Lower	Guadalupe	IV	Medium	3.16
9	N 5.372	W 73.5237	Ventaquemada	Lower	Guadalupe	IV	Medium	2.34
10	N 5.4186	W 73.4545	Tierranegra	Lower	Guadalupe	V	High	1.61
11	N 5.4293	W 73.4501	Puente de Boyacá	Lower	Guadalupe	IV	Medium	3.15
12	N 5.5705	W 73.3292	Tunja	Lower	Bogotá	V	High	1.78
13	N 5.486	W 73.3918	Tunja	Lower	Bogotá	III	Medium	16.70
14	N 5.4917	W 73.3944	Tunja	Lower	Bogotá	III	Medium	5.77
15	N 5.4936	W 73.3979	Tunja	Lower	Bogotá	IV	Medium	3.34
16	N 5.4771	W 73.406	Tunja	Lower	Bogotá	IV	Medium	3.86
17	N 5.4738	W 73.4059	Tunja	Lower	Guadalupe	V	High	3.00
18	N 5.4869	W 73.4041	Tunja	Lower	Guadalupe	V	Medium	2.38
19	N 5.4598	W 73.4193	Puente de Boyacá	Lower	Guadalupe	II	Low	27.70
20	N 5.4443	W 73.4362	Tunja	Middle	Guadalupe	IV	Medium	13.20
21	N 5.4104	W 73.4701	Ventaquemada	Lower	Guadalupe	V	High	1.57
22	N 5.4064	W 73.4764	Ventaquemada	Lower	Bogotá	VI	Medium	0.89
23	N 5.1897	W 73.6204	Villapinzón	Lower	Tilatá	VI	High	0.79
24	N 5.4299	W 73.4499	Villapinzón	Middle	Tilatá	II	Low	23.90
25	N 5.43	W 73.4501	Villapinzón	Lower	Guadalupe	V	Medium	0.62
26	N 5.4013	W 73.4809	Ventaquemada	Lower	Guadalupe	V	High	1.03
27	N 5.3731	W 73.5212	Ventaquemada	Lower	Guadalupe	V	High	1.02
28	N 5.3592	W 73.5358	Ventaquemada	Lower	Guadalupe	IV	Medium	2.27
29	N 5.2865	W 73.5842	Albarracin	Lower	Guadalupe	V	High	1.64
30	N 5.2645	W 73.5864	Chocontá	Lower	Tilatá	IV	Medium	3.18

3. Methodology

3.1. The study area

The study area consists of an 80 km section of the highway that connects Bogotá and Tunja in central Colombia (Fig. 1). This section of the highway was selected for the study because of its varying geologic formations, climatic conditions, and disintegration patterns exhibited by the weak rocks. Different degrees of disintegration could be observed within the same rock type at short distances, adding to the complexity of the disintegration process. Fig. 2 shows a geologic map of the study area, whereas Table 2 shows the ages and lithologic

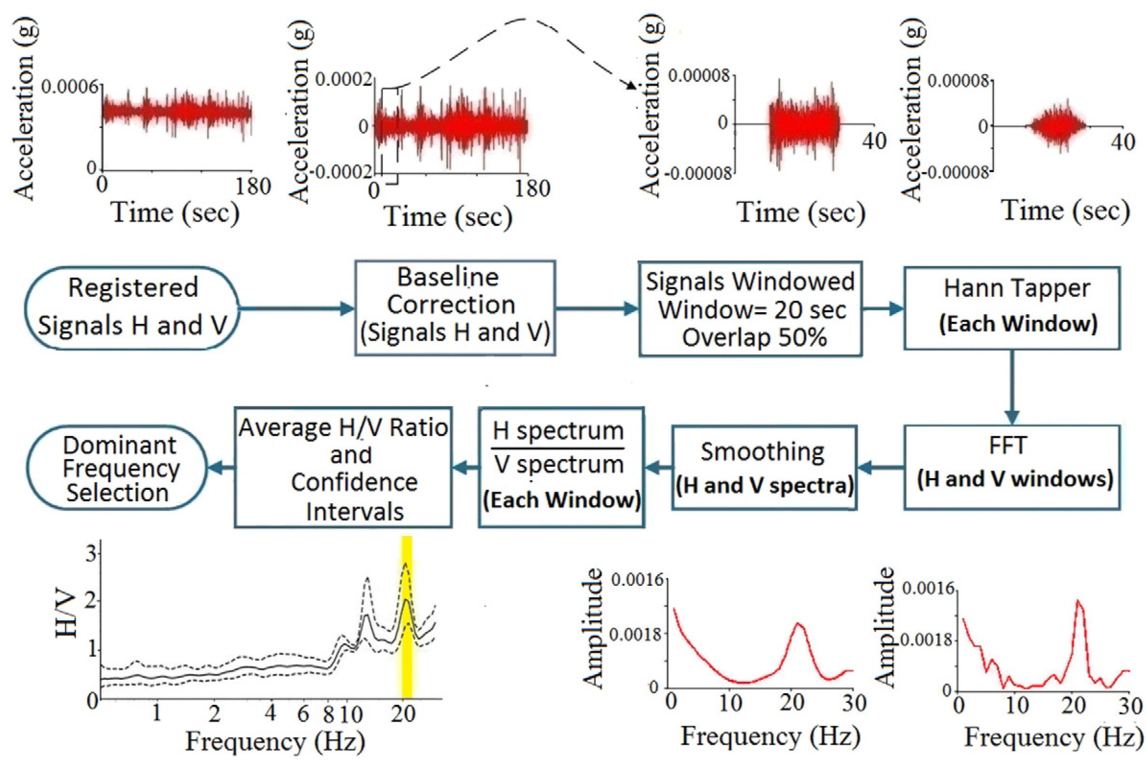

Fig. 3. Flowchart of steps involved in deriving microtremor H/V spectral ratio. The plots above and below the flowchart boxes show examples of different steps.

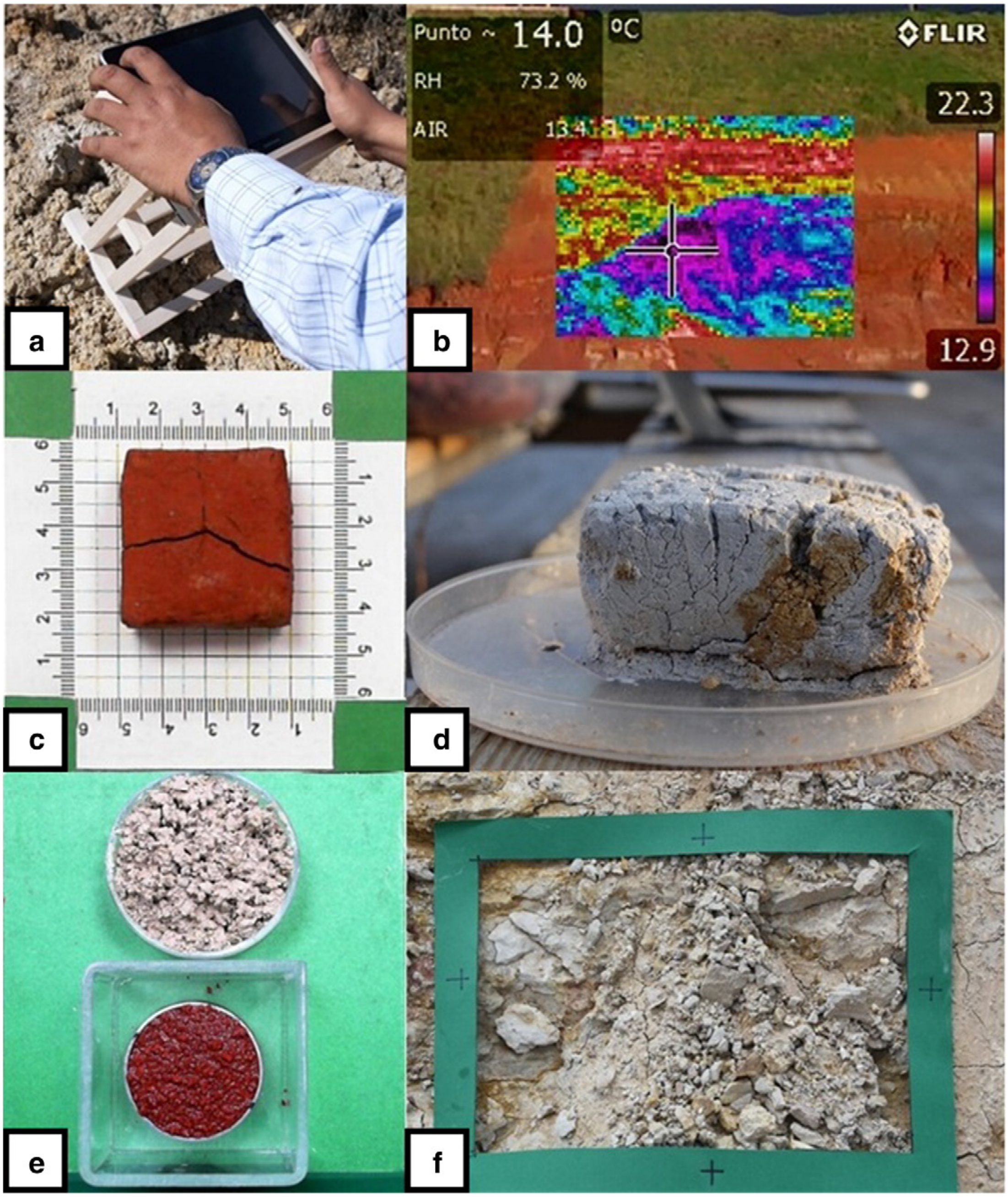

Fig. 4. Examples of image acquisition in both the laboratory and the field: (a) taking an image in the field; (b) infrared image in the field; (c) a fractured bulk fragment after laboratory treatments; (d) block sample exposed to climatic cycles; (e) disintegrated material in the laboratory; and (f) disintegrated material in the field.

composition of various geologic formations exposed along the highway. Thirty-years of data from five climate stations in the study area reveal that the mean annual precipitation varies from 644 mm to 982 mm and the mean temperature ranges between 10.3 °C and 14.4 °C.

3.2. Sampling

Samples for geotechnical characterization of the rocks exposed along the Bogotá–Tunja highway were collected from 38 different sites (Fig. 2). Table 3 provides the locations (Latitudes, Longitudes, and nearby regions referred to as zones), names of geologic formations, and lithologic composition of rock units for the samples collected. Ninety-four block samples, consisting of 49 samples of intact material and 45 samples of material in varying states of disintegration, were obtained. All block samples were carefully wrapped and placed in air-tight containers to avoid damage and moisture alterations. Based on the degree of disintegration, as indicated by SDR (Erguler and Ulusay, 2009), the samples were classified into three disintegration groups: low, medium, and high (Table 4).

Eight (numbers 2, 3, 5, 6, 8, 11, 13, and 18) of the 38 sampling sites, shown in bold in Table 3, were chosen for more detailed monitoring of disintegration progression over time, using image analysis. Two of these sites (numbers 5 and 8) were monitored for disintegration progression for approximately three years from the time of excavation of the cut slopes at these sites. The eight monitoring sites were selected on the basis of their accessibility and lack of any existing or planned structures on them.

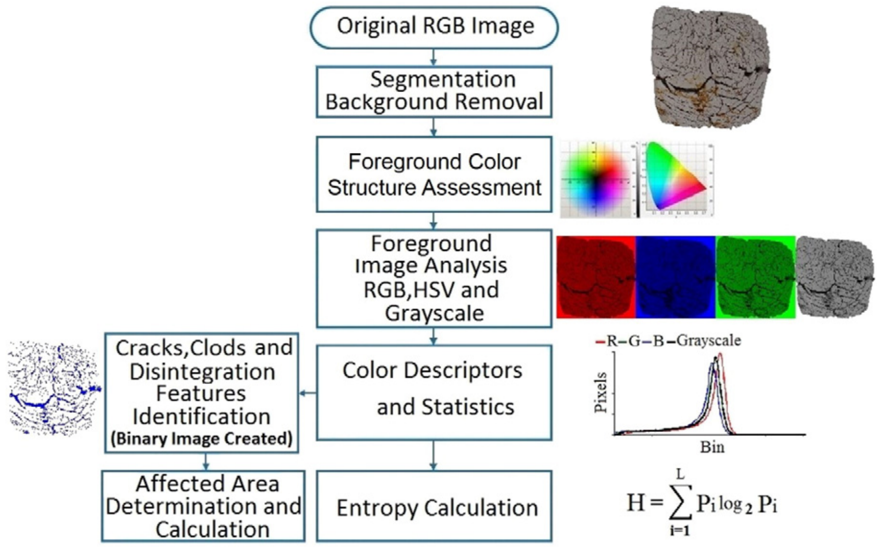

Fig. 5. Flowchart of steps involved in image analysis. The color figures next to the flowchart boxes show examples of different steps.

3.3. Laboratory and field investigations

3.3.1. Geotechnical characterization of rock units

In the laboratory, clay content (0.002 mm and 0.004 mm size material), Atterberg limits (liquid limit, plastic limit, plasticity index), uniaxial compressive strength (UCS), specific surface, bulk unit weight, and second cycle slake durability index (Id_2) were determined for all samples using ASTM procedures (ASTM International., 2013), where applicable. Bulk density and uniaxial compressive strength could not be determined for some low–medium durability samples because of their disintegrated nature, whereas Atterberg limits and specific surface could not be determined for high durability samples because of their hard nature. The specific surface was determined using methylene blue absorption measurements. Clay mineral composition was determined using scanning electron microscopy (SEM-EDS), X-ray diffraction (XRD) analysis, and Fourier transform infrared spectroscopy (FTIR). These tests were performed mainly on samples from Bogotá and Tilatá formations that crop out on the two cut slopes monitored for three years from the date they were cut.

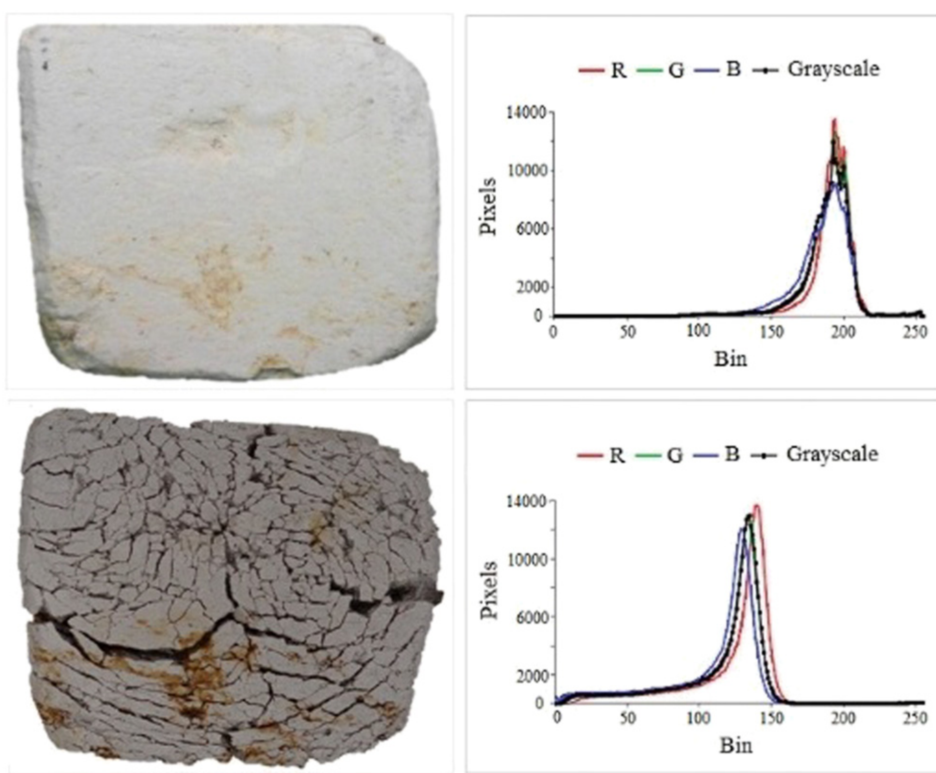

Fig. 6. Red, green, blue, and grayscale histograms (on the right) for a claystone sample: (top) before disintegration and (bottom) after disintegration.

3.3.2. Microtremor measurements

Thirty microtremor measurements were made at selected locations along the Bogotá–Tunja highway. Table 5 provides the locations and related information for the sites used for microtremor measurements. Three accelerometers, Wilcoxon® model 731A, were used to take the measurements. The sampling frequency was 100 MHz and the measurement time was limited to 3 min in order to reduce the effect of external perturbations. The data were processed using GEOPSY software, an open source software for geophysical research and applications (SESAME_Project, 1997, and Seismosignal® software (Seismosoft, 2013). The signals were corrected using a base line correction. The corrected signals were windowed in 20-second lengths with 50% overlap. Over each resulting window, a Hann window tapper filter was applied to reduce border effects due to the cutting process. For each window, fast Fourier transform (FFT) factor was calculated to convert the signal from time domain to frequency domain. The resulting spectrum of each window was smoothed, using the procedure described by Konno and Ohmachi (1998), to remove the small oscillations (noise) from the obtained spectrum. Fig. 3 shows a flowchart of the steps involved in applying the H/V ratio technique to each horizontal and vertical window to derive the desired spectrum. Finally, the H/V ratio between horizontal smoothed spectrum (H) and the vertical smoothed spectrum (V) was calculated for all windows and the average spectrum was calculated with its confidence intervals to get the dominant frequency peak (Fig. 3, bottom left).

3.3.3. Image analysis

Images of varying degrees of disintegration were captured by different commercial cameras: Canon® (10 and 14 Mp), Sony® (18Mp), Nikon® (12 Mp), Samsung® (3 and 5Mp) and Microsoft® (8Mp). The images were taken in both the laboratory and in the field, under diverse conditions of light, distance, distortion, temperature, and moisture content of the material (Fig. 4). In addition, an infrared thermal imaging camera FLIR® was used in some of the experiments for evaluating the moisture zones in the samples. Fig. 5 shows a flowchart of the steps followed in performing image analysis, whereas Fig. 6 shows the red, green, blue, and grayscale histograms for a claystone sample before and after disintegration.

Image analysis was performed using a new algorithm, coded in Microsoft Visual Studio 2013®. First, nine artificial binary images were created, based on the disintegration patterns included in the SDR chart by Erguler and Ulusay (2009). These images were then used to investigate the relationship between entropy (H), mean SDR for each class, mean fracture frequency (λ) , fracture pattern, and affected surface area (Fig. 7). Fig. 7 shows that an increase in entropy indicates a decrease in SDR value, and an increase in fracture frequency (λ) and affected surface area. Second, clay models were made using oil-based clays because they are not affected by moisture changes caused by evaporation, are malleable, and have color stability. These models were used to simulate different disintegration patterns and conditions (Fig. 8). The models allowed sensitivity analysis of image entropy changes under controlled conditions of size, light, color, surface irregularities, and sequence of disintegration. Finally, entropy was calculated for different images taken of laboratory samples and slopes exhibiting different levels of disintegration. For additional information on identifying degradation patterns and morphological features using image analysis of clay models, the reader is referred to Rincón et al. (2014).

SDR Class	SDR Class Mean Value (%)	SDR Class Mean λ (mm^{-1})	Binary Image (Sample Region)	Entropy H (bits)	Affected Surface (%)
IA	100.0	0.00	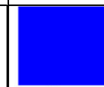	0	0
IB-1	97.5	0.03	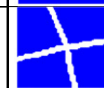	1.183	4.5
IB-2			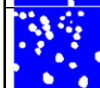	4.3	16.5
II	87.5	0.13		3.676	17.9
III	70.0	0.30	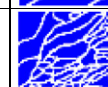	5.5783	27.7
IV	50.0	0.50		6.475	36.2
V	30.0	0.70	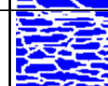	7.357	44.4
VI-1	10.0	0.90	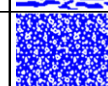	6.41	34.5
VI-2				7.67	54.6

Fig. 7. Relationship between entropy (H), mean value of SDR, mean fracture frequency (**λ**), disintegration patterns, and affected surface area, based on image analysis.

4. Results

4.1. Laboratory test results

Table 6 presents the geologic and engineering properties of the samples tested. Generally speaking, low–medium durability samples are characterized by higher clay content, higher plasticity index, higher specific surface, lower UCS, and lower Id_2 values compared to high durability samples. Based on the correlation between Atterberg limits and clay mineralogy, developed by Mitchell (1993) and shown in Fig. 9, the likely clay minerals present in the samples tested include kaolinite, illite, and montmorillonite. Fig. 9 also shows the relationship between SDR classes for the samples tested and clay mineralogy. The relationship is rather inconsistent and inconclusive, indicating that clay mineralogy is not the only property influencing the degree of disintegration. The correlation between specific surface and clay mineralogy, proposed by Santamarina et al. (2002) with data from Mitchell (1993), suggests the presence of illite and kaolinite (Fig. 10). Fig. 10 shows that most medium and high durability samples contain illite as the dominant clay mineral but the relationship between SDR class and specific surface is inconclusive, again suggesting that multiple factors influence the degree of disintegration. The SEM, XRD, and FTIR analyses confirmed the preliminary, correlation-based results of clay mineralogy.

4.2. Microtremor measurement results

Table 5 shows the degree of disintegration and the estimated fundamental frequency, also termed the dominant frequency, obtained from H/V spectral ratio signal for each of the 30 sites where microtremor readings were taken. Microtremor measurements were made at sites with low, medium, and high degrees of disintegration, in accordance with the classification shown in Table 4. In terms of the SDR classes, the sites fall between SDR class II and SDR class VI. None of the slopes along the highway received SDR of class I because of significant disintegration observed in the field, even for slopes that had been cut relatively recently. Fig. 11, based on data in Tables 1 and 5, shows the variation of fundamental frequency with respect to fracture frequency (λ), SDR class, and low, medium, and high degrees of disintegration. The fundamental frequency of H/V spectral ratio generally decreases as the

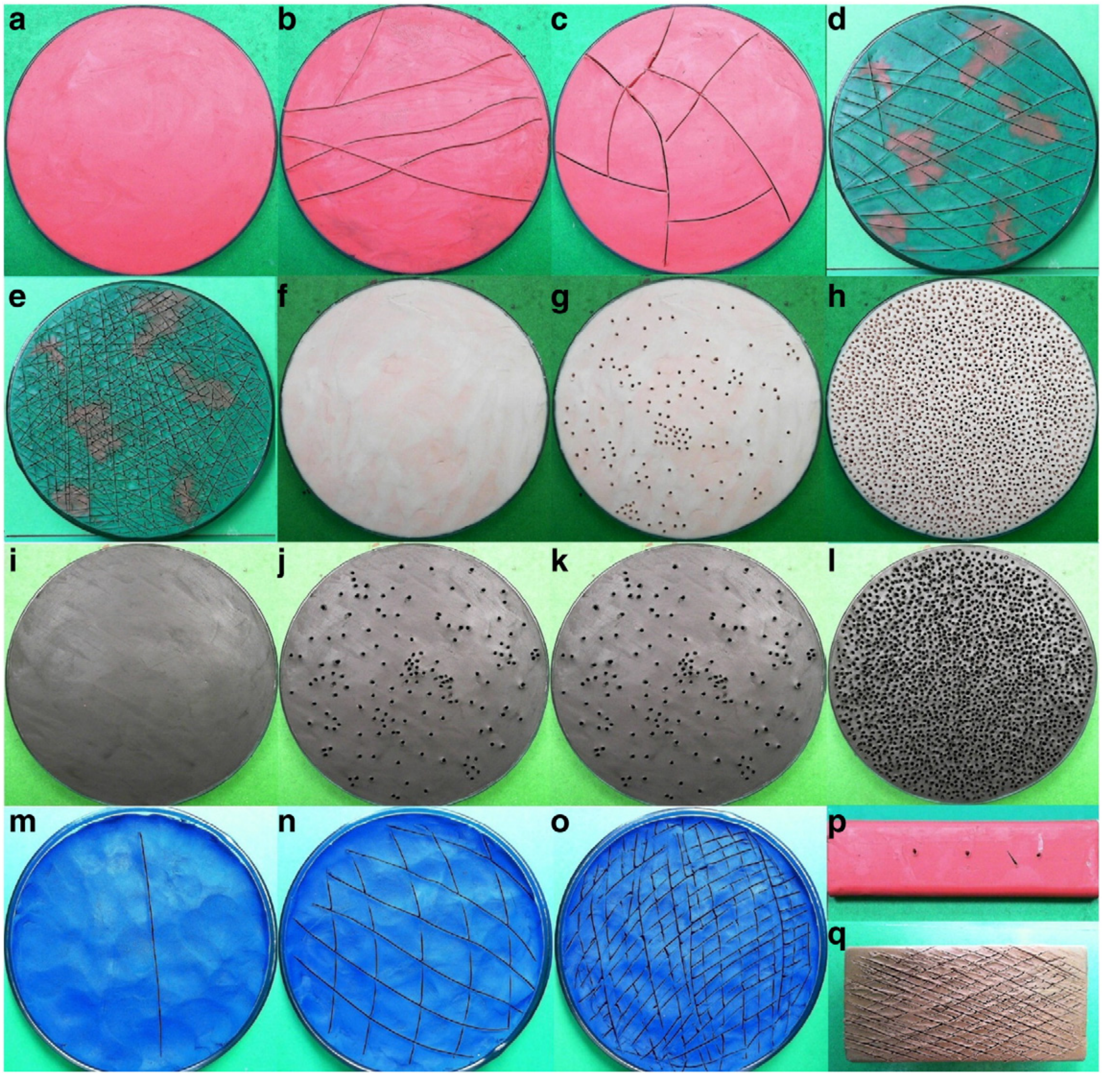

Fig. 8. Example of some clay models used to simulate different states of disintegration, different colors, and different initial textures: (a), (b) and (c) models with cracks in the same color (red); (d) and (e) models with cracks in mottled color; (f) model with no holes; (g) through (l) models with holes to represent different textures in lighter and darker grays; (m), (n), and (o) models with varying crack patterns in the same color (blue); (p) and (q) bulk models with holes or cracks.

fracture frequency and degree of disintegration increase. Note that the variations of fundamental frequency with respect to the five SDR classes (II to IV), shown in Fig. 11, are due to the fact that the data are arranged with respect to SDR classes based on fracture frequency (λ), not with respect to fundamental frequency. Thus, the variations within each class reflect the subjectivity of human observation in characterizing the fracture frequency. This suggests the need for developing independent classifications based on instrumental techniques, such as microtremor measurements and image analysis, for characterizing the degree of disintegration. Fig. 12 shows a plot of the mean fundamental frequency of H/V spectral ratio versus the mean SDR value for various SDR classes (Tables 1 and 5). The exponential relationship in Fig. 12 has a high correlation coefficient (R^2) of 0.99, suggesting that H/V spectral ratio can be a reliable means of assessing the degree of disintegration of weak rocks.

4.3. Image analysis results

Fig. 13 shows the theoretical relationship between entropy values obtained from the binary images, created to simulate the fracture patterns corresponding to SDR classes (Fig. 7), and the mean fracture frequency (λ) for each pattern (Table 1). Since the SDR chart by Erguler and Ulusay (2009) uses two patterns each for the classes IB and VI, the subindices 1and 2 are used in Fig. 13 to identify these patterns (IB-1, IB-2), VI-1, VI-2). The figure shows that the range of possible entropy values for SDR classes is 0–8. The figure also shows that two of the suggested patterns in the SDR classification system, i.e. classes I B-2 and VI-1, do not follow the same trend as the other seven SDR classes or patterns. A possible explanation for this could be that the SDR patterns are based on the presence of only visible cracks captured by a binary image and do not consider such textural features as microcracks, voids, and other irregularities. These textural features are too small to be observed by the human eye but can be captured by the high resolution camera lens.

Fig. 14 shows the images of some disintegrated rock material and clay models, with their entropy values. The minimum value of entropy measured for clay models was 4.84 bits (image 2, Fig. 14). For rock samples, the minimum entropy value was around 5 bits, as obtained from images of different rock fragments carefully selected during excavations. Images 3 and 6 in Fig. 14 show carved samples, with entropy values of 5.89 bits for the image with edges (image 3), and 5.39 bits for the image without edges (image 6), indicating that edges result in an increase in entropy. Image 9 in Fig. 14 shows the same sample as in images 3 and 6 but after five days of exposure to natural climatic conditions during July of 2014, with the entropy increasing to 6.46 bits. Image

Table 6
Geologic and engineering properties of the samples tested.

Sample ID	Site	Disintegration level	4 μm-clay (%)	2 μm-clay (%)	Liquid limit	Plastic limit	Plasticity index	Compressive strength (kPa)	Specific surface m^2/g	Bulk unit weight (kN/m^3)	Second cycle slake durability index (Id_2) (%)
1	1	Low	18.50	17.50	62.1	23.8	38.3		348.64		
2	1	Medium	45.00	43.00	71.5	16.7	54.8		122.33		
3	2	High							61.17		
4	2	Medium							61.17		2
5	2	Medium							79.52		0
6	2	Low			47.5	16.2	31.3		61.17		
7	3	Medium			65.6	25.5	40.1		61.17		
8	3	Medium			114	26	88		61.17		
9	3	Medium	49.00	43.60	57	25	32		61.17		
10	3	High			52.1	24	28.1		79.52		
11	3	Medium			74.1	29	45.1		61.17		
12	4	Low	54.00	50.60	61.5	24.4	37.1		152.91		
13	4	High	75.70	75.00	93	25	68		152.91		
14	4	Medium	86.00	85.00	87	24.5	62.5		152.91		
15	5	Medium	94.00	92.70	58.5	35	23.5		110.10		2
16	5	High	90.40	90.40	92.4	35.3	57.1		91.75		
17	5	High			71.3	34	37.3		61.17		
18	7	Medium			36	13.3	22.7		91.75		0
19	7	Medium	69.00	60.00	53	14.7	38.3		116.21		0
20	7	Medium			58	18	40		30.58		1
21	8	High			36.8	15.3	21.5		91.75		0
22	8	High			32.9	12	20.9				17
31	26	Low								19.3	17
32	26	Low	43.50	41.00	55.2	27.24	28	449	17.37	20.1	
33	26	Low						463		17.2	
34	26	Low						1525		16.0	15
35	25	Low	43.50	41.00	35.4	17.2	18.2	367	17.43	20.9	
36	25	Low						311		21.1	
37	25	Low						285		18.7	
38	25	Medium						395		18.2	
39	25	Medium						76		16.6	
40	6	Medium	71.00	30.00	67.3	38.79	28.6	77		17.3	
41	6	Medium						107	17.13	15.6	
42	6	High						94		20.3	
43	15	High	37.50	27.50	32.6	15.71	16.9	69	17.80	17.3	
44	15	Medium						93		15.4	
45	15	Low						350		20.8	
46	15	Low						758		23.8	
47	14	Low	66.00	34.00	52.4	28.81	23.6	680	17.13	22.8	
48	14	Low						376		20.8	
49	8	Low	18.50	16.40	28.6	15.22	13.4		16.45	20.7	17
51	8	Low								22.9	
52	11	Medium	36.50	25.00	38.6	21.43	17.2	119	17.07	21.9	
53	11	Medium						159		19.9	
55	11	Low								21.5	
57	11	Medium						5895		22.2	20
58	3	Medium						665		18.4	17
59	11	Low						14,667		23.3	
60	6	Medium						1497		19.8	
61	8	Low			41	20.9	20.1	10,519		23.1	
62	13	Medium						450		20.5	
63	13	High			34	16.4	17.6	319		20.1	
64	13	High						251		20.8	
65	13	High			40	26.6	13	412		19.9	
66	13	Medium			32	16.1	16	611		20.6	
67	33	High			43	15.2	27.8	322		20.6	
68	33	High						166		20.4	
69	33	High						215		20.5	
70	33	High			29	19	10	450		22.5	
71	37	High						217		19.6	
72	37	High						217		21.2	
73	37	High			44	15.1	28.9	217		21.4	
74	22	High						210		19.6	
75	22	High						202		19.6	
76	22	High						204		19.7	
77	22	High			49	23.3	25.7	184		19.7	
78	22	Medium			45	21.8	23.2	713		21.9	
79	22	Medium			48	22.2	25.8	843		22.2	
80	27	High			48	23	25	454		19.5	
81	27	High						700		22.0	
82	27	High			59	25.7	33.3	100		16.5	
83	27	High						172		17.3	

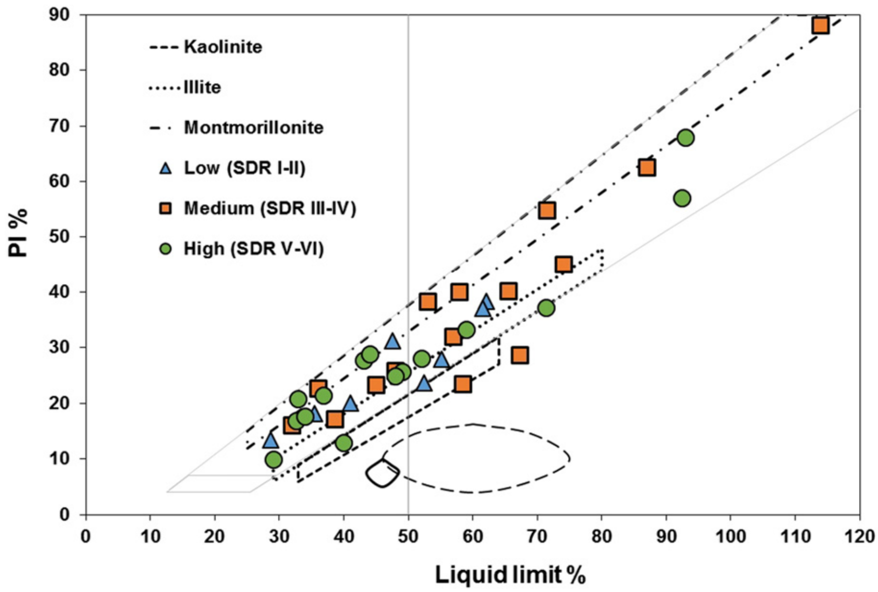

Fig. 9. Casagrande plasticity chart showing clay mineralogy and SDR values of the samples tested in relation to Atterberg limits. Modified from Mitchell (1993).

12 shows the same material in the field two months after the excavation was made; the entropy is 7.1 bits. Image 15 in Fig. 14 shows the same sample after 26 months with entropy increasing to 7.5, whereas image 18 was taken 32 months after excavation and the entropy increased to 7.7 bits. These results show that entropy increases with increasing degree of disintegration. Images 8, 14 and 17, from the Bogotá Formation, show similar results.

Clay models were found to be quite useful in simulating surface features such as cracks, voids, and other irregularities that influence entropy. The blue, black, gray, and green models in Fig. 15 refer to different color clay models used in the study such as those shown in Figs. 8 and 14. The purpose was to verify that increase in entropy with small changes in the clay model surfaces was uniform and the trends were consistent across colors. Such consistency is important if entropy is to be used for monitoring progression of disintegration under different light conditions, as influenced by the color of material. Fig. 15 shows the results from four different clay models with different colors and initial surface conditions. Disintegration was simulated by making an increasing number of holes with a 1-mm diameter needle. Image 5 in Fig. 14 shows the entropy for one of those samples. The four trend lines in Fig. 15 show that the maximum possible value of entropy is 8 bits when the affected surface is about 26.5% of the entire surface area of the sample.

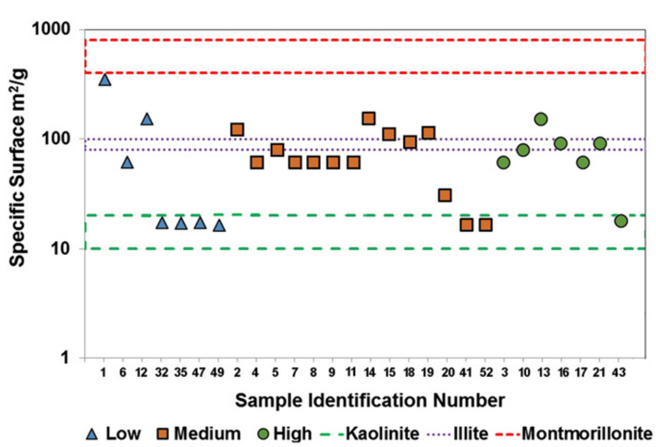

Fig. 10. Relationship between specific surface, clay mineralogy, and varying degrees (low, medium, and high) of disintegration. The green, purple, and red horizontal bands indicate the ranges of specific surface for kaolinite, illite, and montmorillonite, respectively. Modified from Mitchell (1993) and Santamarina et al. (2002).

5. Discussion

The fundamental frequency values derived from H/V ratios (Table 5) are related to varying degrees of disintegration (Fig. 11). The

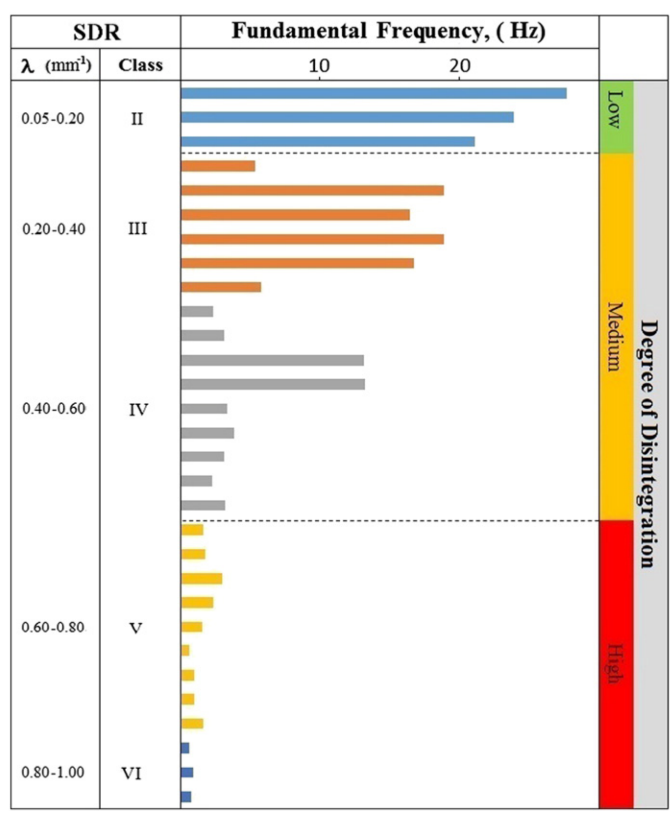

Fig. 11. Variation of dominant frequency in relation to mean fracture frequency (λ) and degree of disintegration expressed in terms of SDR and low, medium, and high classes.

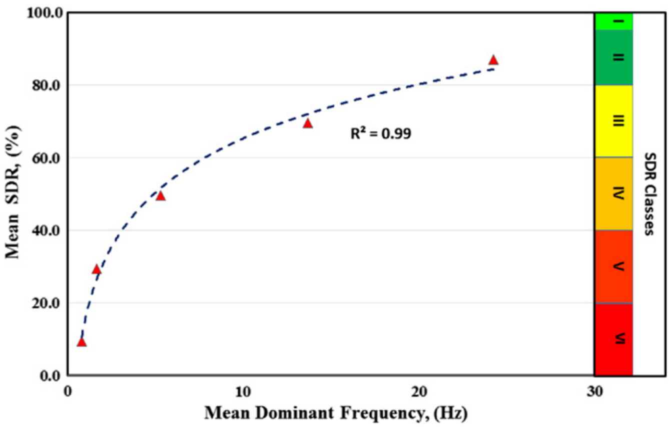

Fig. 12. Relationship between dominant frequency, based on H/V ratio, and SDR.

fundamental frequency bands corresponding to low, medium, and high disintegration classes are 21.1–27.7 Hz (average 24.2 Hz), 2.27–18 Hz (average 8.7 Hz), and 0.65–3 Hz (average 1.4 Hz), respectively. These results suggest a definite relationship between the extent of disintegration of a weak rock and its low-strain dynamic behavior (i.e. response to microtremors). The change in frequency is caused by the reduction of rock mass stiffness upon disintegration. The process of disintegration begins at the exposed surface and progresses inward. Thus, the dynamic response of near surface material is different than the dynamic response of the interior of the rock mass. This contrast in the stiffness and dynamic response between the outer and inner zones enables one to obtain a spectral transference function between unslaked and slaked portions of the cut slope. Therefore, potentially, the H/V ratio can be used for differentiating between different degrees of disintegration. Low frequency values indicate soil-like materials, high frequency values indicate rock-like materials, and intermediate frequency values indicate intermediate materials (IGMs) between soil and rock.

The dynamic response corresponding to varying degrees of slaking observed in this study agrees with results reported by Arroyo et al. (2010) who studied shear wave propagation through argillaceous rock cores exhibiting varying degrees of disintegration. The strong correlation ($R^2 = 0.99$) between fundamental frequency and SDR, as shown in Fig. 12, suggests that the frequency derived from H/V ratio, using microtremors, can be a reliable, quick, and economical tool for characterizing and quantifying the disintegration behavior of weak rocks in the field.

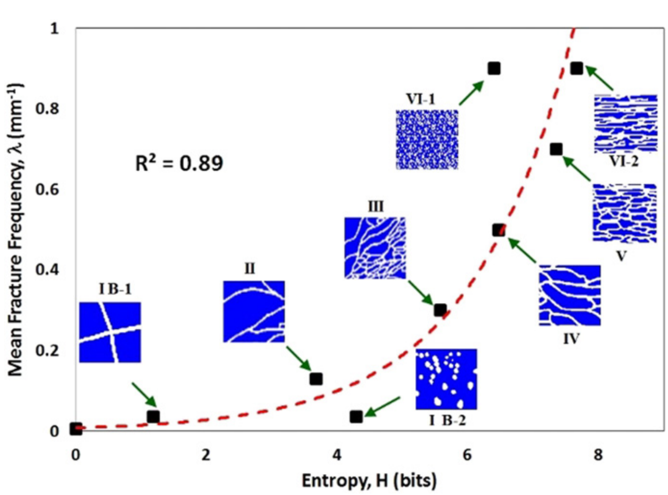

Fig. 13. Relationship between image entropy, fracture frequency, and SDR class.

The current ASTM standard method for slake durability test for shales and similar weak rocks (ASTM D4644; ASTM International, 2013) requires that photographs of the specimen be taken before and after the test. These photographs are used for description and comparison purposes but not for analysis. In this research, we reviewed different image descriptors and chose the image entropy because it reflects the changes in color intensities in an image, which makes it an appropriate tool for characterizing and monitoring disintegration. This research demonstrates that colors (red, green, and blue) change when surface conditions change due to an increasing degree of disintegration (Fig. 6). The changes in color are reflected in the shape of the corresponding histograms, with higher intensity colors indicating higher entropy. The changes in color intensities are associated with changes in the quantity of light absorbed with more light being absorbed by disintegrated material due to an increase in void space.

Image entropy is unaffected by changes in the position of the camera because the entropy quantifies only the light reflectance, not the position of the disintegrated material in the image. This makes entropy a versatile parameter to be used in the field without requiring specific orientations of the images. Another advantage of this technique as a field tool is the high resolution of digital cameras, tablets, and phones which makes it possible to detect very low degrees of disintegration in great detail at scales below 2 mm — the mesh size of the drum used for the slake durability test. Therefore, image entropy can be used as a very useful descriptor of the disintegration state.

The above discussion shows that H/V spectral ratio and image entropy are reliable means of assessing and quantifying the degree of disintegration, as expressed by the SDR classes proposed by Erguler and Ulusay (2009). However, application of the SDR classification is based on human observations and can be subjective.

It should be noted that the image analysis technique was not applied to all of the field sites where H/V ratios were measured. Most of the image analysis was done on laboratory samples. Therefore, a relationship between entropy H and dominant frequency of H/V ratio could not be established for the study sites. For H/V ratio and image entropy to provide a more meaningful and unbiased categorization of the degree of disintegration of weak rocks, future research should be oriented toward developing an independent classification of the degree of disintegration based entirely on these two instrumental parameters. This would require establishing a relationship between entropy H and dominant frequency of H/V ratio.

6. Conclusions

The following conclusions can be drawn from this study:

1. Dominant frequency, based on H/V spectral ratio derived from microtremor measurements, and image entropy are reliable parameters for quantifying varying degrees of disintegration of cut slopes in weak rocks. The two parameters, in combination, can differentiate reliably between materials of low, medium, and high degrees of disintegration. Rocks exhibiting a low degree of disintegration are characterized by dominant frequency values of more than 19 Hz and entropy values of less than 6 bits, those with a medium degree of disintegration have frequency values between 19 and 3 Hz and entropy values between 6 and 7 bits, and rocks that have a high degree of disintegration have frequencies below 3 Hz and entropies above 7 bits.
2. The image analysis technique can be used to reliably differentiate between slaking characteristics of laboratory samples of different weak rocks.
3. Future work should focus on developing an independent classification of disintegration degree based on the relationship between H/V ratio and image entropy.

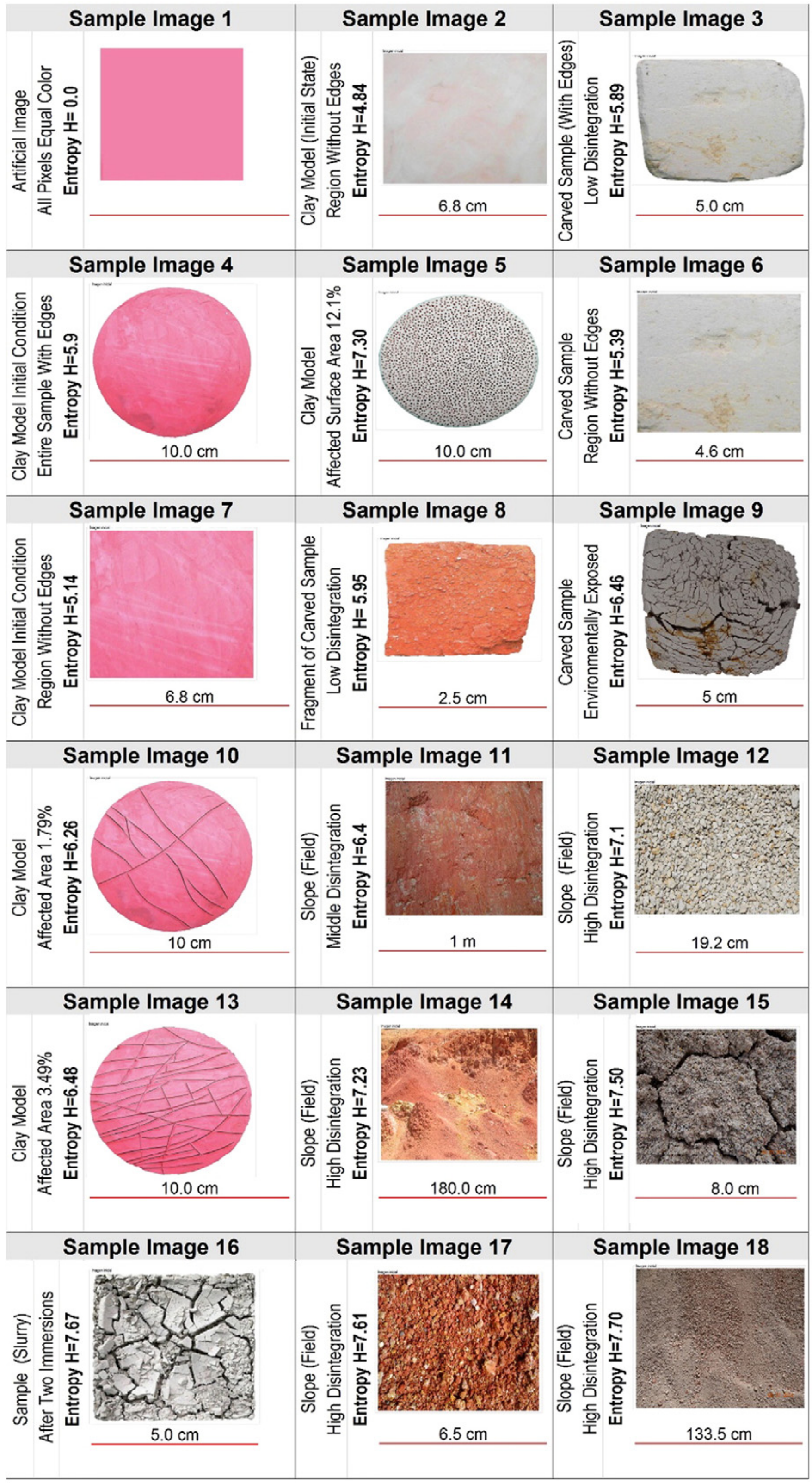

Fig. 14. Images of different materials and clay models, exhibiting different conditions, and the corresponding entropy values.

Acknowledgments

The first author acknowledges COLCIENCIAS (Administrative Department of Science, Technology, and Innovation, Colombia) for the financial support he received through "Generación Del Bicentenario" Ph.D. scholarship programs well as the field and laboratory assistance received from the Pontificia Universidad Javeriana. Thanks are also due to Clairet Guerra who helped in microtremor measurements in the field.

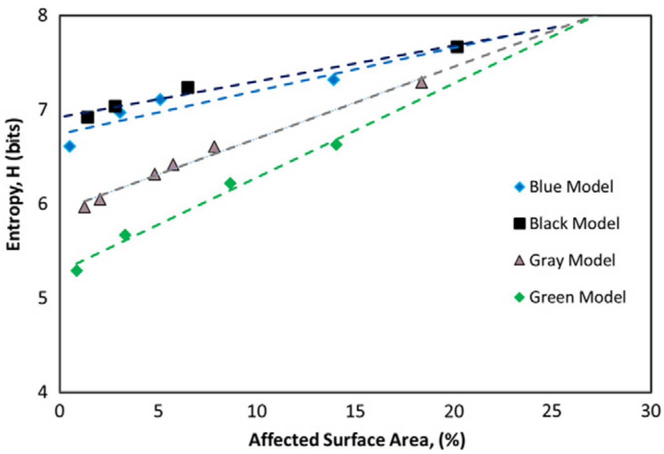

Fig. 15. Entropy versus affected surface area for different initial states of clay models.

References

Arroyo, M., Pineda, J., Romero, E., 2010. Shear wave measurements using bender elements in argillaceous rock. Geotech. Test. J. 33. http://dx.doi.org/10.1520/GTJ102872.

ASTM International, 2013. Annual book of ASTM standards 2013: construction. Soil and Rock (I): D420–D5876. Section 4. Vol. 04.08. ASTM International (1826 p).

Burger, W., Burge, M.J., 2013. Principles of Digital Image Processing: Advanced Methods. Springer.

Clavero, D., Rosa-Cintas, S., López-Casado, C., Delgado, J., Galiana-Merino, J.J., 2014. Shear wave velocity estimation in the metropolitan area of Málaga (S Spain). J. Appl. Geophys. 109, 175–185.

Cruz, N., Fonseca, A.V.D., Rodrigues, C., 2012. A specific protocol to characterize Intermediate Geomaterials (IGM). Geotechnical and Geophysical Site Characterization 4. CRC Press, pp. 985–992.

Czerewko, M.A., Cripps, J.C., 2001. Assessing the durability of mudrocks using the modified jar slake index test. Q. J. Eng. Geol. Hydrogeol. 34, 153–163. http://dx.doi.org/10.1144/qjegh.34.2.153.

Delgado, J., López Casado, C., Estévez, A., Giner, J., Cuenca, A., Molina, S., 2000. Mapping soft soils in the Segura river valley (SE Spain): a case study of microtremors as an exploration tool. J. Appl. Geophys. 45, 19–32.

Dinc, O.S., Sonmez, H., Tunusluoglu, C., Kasapoglu, K.E., 2011. A new general empirical approach for the prediction of rock mass strengths of soft to hard rock masses. Int. J. Rock Mech. Min. Sci. 48, 650–665.

Dinesh, B.V., Nair, G.J., Prasad, A.G.V., Nakkeeran, P.V., Radhakrishna, M.C., 2010. Estimation of sedimentary layer shear wave velocity using micro-tremor H/V ratio measurements for Bangalore city. Soil Dyn. Earthq. Eng. 30, 1377–1382.

Erguler, Z.A., Shakoor, A., 2009. Relative contribution of various climatic processes in disintegration of clay-bearing rocks. Eng. Geol. 108, 36–42.

Erguler, Z.A., Ulusay, R., 2009. Assessment of physical disintegration characteristics of clay-bearing rocks: disintegration index test and a new durability classification chart. Eng. Geol. 105, 11–19.

Gautam, T., Shakoor, A., 2013. Slaking behaviour of clay-bearing rocks during a one-year exposure to natural climatic conditions. Eng. Geol. 106 (1), 17–25.

Goodman, R.E., 1989. Introduction to Rock Mechanics. Wiley.

Guéguen, P., Chatelain, J.L., Guillier, B., Yepes, H., 2000. An indication of the soil topmost layer response in Quito (Ecuador) using noise H/V spectral ratio. Soil Dyn. Earthq. Eng. 19, 127–133.

Guo, Z., Aydin, A., Kuszmaul, J.S., 2014. Microtremor recordings in Northern Mississippi. Eng. Geol. 179, 146–157.

Harutoonian, P., Leo, C.J., Doanh, T., Castellaro, S., Zou, J.J., Liyanapathirana, D.S., Wong, H., Tokeshi, K., 2012. Microtremor measurements of rolling compacted ground. Soil Dyn. Earthq. Eng. 41, 23–31.

Heilbronner, R., Barrett, S., 2013. Image Analysis in Earth Sciences: Microstructures and Textures of Earth Materials. Springer.

ISRM, 2007. The complete ISRM suggested methods for rock characterization, testing and monitoring: 1974–2006. In: Ulusay, R., Hudson, J.A. (Eds.), Suggested Methods Prepared by the Commission on Testing Methods. International Society for Rock Mechanics, Compilation Arranged by the ISRM Turkish National Group, Ankara, Turkey.

Kanai, K., Tanaka, T., 1961. On microtremors. Bull. Earthquake Res. Inst. 39, 97–114.

Konno, K., Ohmachi, T., 1998. Ground-motion characteristics estimated from spectral ratio between horizontal and vertical components of microtremor. Bull. Seismol. Soc. Am. 88, 228–241.

Marinos, P., Hoek, E., 2000. GSI—a geologically friendly tool for rock mass strength estimation. GeoEng2000 Conference, Melbourne, pp. 1422–1446.

Mitchell, J.K., 1993. Fundamentals of Soil Behavior. second ed. Wiley, New York.

Mokwa, R., Brooks, H., 2008. Axial Capacity of Piles Supported on Intermediate Geomaterials. Montana Departament of Trasportation.

Mokwa, R., Brooks, H., 2009. Driven pile capacity in intermediate geomaterial formations. Contemporary Topics in Deep Foundations. American Society of Civil Engineers, pp. 263–270.

Mundepi, A.K., Galiana-Merino, J.J., Kamal, Lindholm, C., 2010. Soil characteristics and site effect assessment in the city of Delhi (India) using H/V and f–k methods. Soil Dyn. Earthq. Eng. 30, 591–599.

Nakamura, Y., 1989. A method for dynamic characteristics estimation of subsurface using microtremor on the ground surface. Qual. Rep. 30, 25–33.

Nakamura, Y., 2000. Clear identification of fundamental idea of Nakamura's technique and its applications. In: Engineering, N.Z.S.f.E. (Ed.), 12 WCEE. New Zealand Society for Earthquake Engineering, Auckland, New Zealand, p. 8.

Ojeda, A., Escallon, J., 2000. Comparison between different techniques for evaluation of predominant periods using strong ground motion records and microtremors in Pereira Colombia. Soil Dyn. Earthq. Eng. 20, 137–143.

Ojeda, A., Martinez, S., Bermudez, M., Atakan, K., 2002. The new accelerograph network for Santa Fe De Bogota, Colombia and implications for microzonation. Soil Dyn. Earthq. Eng. 22, 791–797.

Parolai, S., Richwalski, S.M., Milkereit, C., Bormann, P., 2004. Assessment of the stability of H/V spectral ratios from ambient noise and comparison with earthquake data in the Cologne area (Germany). Tectonophysics 390, 57–73.

Peck, R.B., Hanson, W.E., Thornburn, T.H., 1974. Foundation Engineering. 2d ed. Wiley, New York.

Rincón, O., Florez, L., Ocampo, M.S., 2014. Clay-bearing rocks slaking characterization using artificial vision. Geomechanics from Micro to Macro. CRC Press, pp. 1473–1477.

Ritta, R.J., Massa, J.C., Chiappero, G.D., 2013. Processing of ambient vibration records for the estimation of the fundamental vibration period of soil deposits. Latin America transactions. IEEE (Rev. IEEE Am. Lat.) 11, 300–306. http://dx.doi.org/10.1109/tla.2013.6502820.

Rosenblad, B.L., Goetz, R., 2010. Study of the H/V spectral ratio method for determining average shear wave velocities in the Mississippi embayment. Eng. Geol. 112, 13–20.

Sadisun, I.A., Shimada, H., Ichinose, M., Matsui, K., 2005. Study on the physical disintegration characteristics of Subang claystone subjected to a modified slaking index test. Geotech. Geol. Eng. 23, 199–218. http://dx.doi.org/10.1007/s10706-003-6112-6.

Samtani, N., Nowatzki, E., 2006. Soils and Foundations Reference Manual. Federal Highway Administration.

Santamarina, J.C., Klein, K.A., Wang, Y.H., Prencke, E., 2002. Specific surface: determination and relevance. Can. Geotech. J. 39, 233–241. http://dx.doi.org/10.1139/t01-077.

Santi, P.M., 1998. Improving the jar slake, slake index, and slake durability tests for shales. Environ. Eng. Geosci. 4, 385–396.

Santi, P.M., 2006. Field methods for characterizing weak rock for engineering. Environ. Eng. Geosci. 12, 1–11. http://dx.doi.org/10.2113/12.1.1.

Seismosoft, 2013. SeismoSignal Seismosoft, Pavia Italy, Package for the Processing of Strong-Motion Data.

SESAME_Project, 1997. Open source software for geophysical research and applications. In: geopsy.org (Ed.), Geopsy.Org Applications. Geopsy.org, Grenoble.

Shannon, C., 1948. A mathematical theory of communication. Bell Syst. Tech. J. 27.

Siddiqqi, J., Atkinson, G.M., 2002. Ground-motion amplification at rock sites across Canada as determined from the horizontal-to-vertical component ratio. Bull. Seismol. Soc. Am. 92, 877–884. http://dx.doi.org/10.1785/0120010155.

Sukumaran, P., Parvez, I.A., Sant, D.A., Rangarajan, G., Krishnan, K., 2011. Profiling of late Tertiary–early Quaternary surface in the lower reaches of Narmada valley using microtremors. J. Asian Earth Sci. 41, 325–334.

Tonnizam, E., Saad, R., Vahid, S., 2011. Durability assessment of weak rock by using jar slaking test. Electron. J. Geotech. Eng. 16.

Vella, A., Galea, P., D'Amico, S., 2013. Site frequency response characterisation of the Maltese islands based on ambient noise H/V ratios. Eng. Geol. 163, 89–100.

Walling, M.Y., Mohanty, W.K., Nath, S.K., Mitra, S., John, A., 2009. Microtremor survey in Talchir, India to ascertain its basin characteristics in terms of predominant frequency by Nakamura's ratio technique. Eng. Geol. 106, 123–132.

Zaslavsky, Y., Shapira, A., Arzi, A.A., 2000. Amplification effects from earthquakes and ambient noise in the Dead Sea rift (Israel). Soil Dyn. Earthq. Eng. 20, 187–207.